Post–Dryout Heat Transfer in Straight and Curved Tubes

G. Lautenschlager, F. Mayinger
Institute A for Thermodynamic
Technical University of Munich

prepared for the

Second International Workshop on
Two–Phase Flow Fundamentals

Post–Dryout Heat Transfer in Straight and Curved Tubes

G. Lautenschlager, F. Mayinger
Institute A for Thermodynamic
Technical University of Munich

1. Background

Post dryout heat transfer occurs at high void fractions, when the liquid phase is no longer able to wet a heated wall. In this so called dispersed flow the liquid phase is distributed as entrained droplets in a more or less superheated vapour bulk.
In recent years, a large amount of research has been done in this field, motivated by engineering needs in thermohydraulics of nuclear reactor safety. Most of the experimental work has been carried out in straight, mainly in vertical tubes. However, every equipment contains tube bends and steam generators often consist of helically coiled tubes, wherein large centrifugal forces and separation effects occur.
The experiments carried out in curved tubes at the Institute A for Thermodynamic have two aims:
The first aim is to research the local distribution of heat transfer coefficient along the circumference of curved tubes. The second one is to vary the traverse droplet motion and the droplet concentration in the cross section by different centrifugal forces, in order to get more information about the mechanisms for post dryout heat transfer.
It was for these reasons that the experiments were carried out systematically at different pressure ratios, mass flow rates, heat flux densities and diameter ratios.
Though the emphasis of this work is the curved tube, we are able to contribute also data sets for the straight tube, because – upstream of the bend – we have a straight vertical inlet section where the dryout occurs.

2. Description of apparatus and test section

The experiments presented were carried out in a refrigerant R 12 loop ($T_{crit} = 111.8°C$, $p_{crit} = 41.2\ bar$), which is shown in figure 1. The main components of the loop are a centrifugal pump, a preheater, an evaporator, the test section and a condenser. The test section, mainly consisting of a straight vertical tube and a joined 90°– bend or a 450° – coil, respectively is shown in figure 2. The tube is made of stainless steel with an inner diameter of 28.5 mm and an outer diameter of 33.7 mm. The wall thickness in the straight tube varies within ± 0.04 mm (1.5% of wall thickness). Differences in wall thickness of the curved tube resulting from bending range between 0.03 and 0.12 mm (1.2 ÷ 4.6%). The total height of the test section is 4.06 m. Depending on the diameter of curvature of the bend, the length of the straight tube varies between 3.86 m and 3.45 m. The test tube is uniformly heated by DC. The quality $\dot{x}$ at the test section inlet is adjusted by the electrically heated evaporator in such a way that the dryout in the vertical tube always

occurs about 2.5 m before the bend inlet yielding flow conditions as shown in fig. 3. All heated components, such as preheater, evaporator and test section are insulated with glass fiber material, with a thermal conductivity of 0.035 W/mK and a thickness of 30 mm. In this way heat losses are reduced considerably.

Flow Rate Measurement

Mass flow rate is determined in subcooled liquid flow by measuring the pressure drop across an orifice. Two parallel orifice sections are used for better accuracy, one with a 11 mm – diameter and the other with a 16 mm – diameter orifice. Flow is directed through either line, depending on flow rate. Flow rate is calculated with equation (1):

$$\dot{m} = \alpha \cdot A_0 \sqrt{2\rho_l \Delta p} \tag{1}$$

$$\begin{aligned} \dot{m} &= mass\ flow\ rate\ [kg/s] \\ A_0 &= cross\ section\ of\ orifice\ [m^2] \\ \rho_l &= liquid\ density\ [kg/m^3] \\ \Delta p &= pressure\ drop\ [Pa] \\ \alpha &= coefficient \end{aligned}$$

The coefficient α was determined by calibrating each orifice with water in a large range of Reynolds numbers. The small and large orifices yield constant coefficients $\alpha = 0.61$ and 0.62, respectively with an uncertainty of 0.5 percent. The pressure drop Δp is measured by a differential pressure transducer (Burster type A5) with an uncertainty of $\pm$ 0.5 percent of full scale. Liquid density ρ_l is calculated from fluid temperature.

Pressure Measurement

Absolute pressure is measured at the inlet of the test section with a pressure transducer (type Burster 821.1 RS) basing on strain gauge technique. The measuring range is 0 to 50 bar with uncertainties associated with hysteresis and nonlinearity of $\pm$ 0.25 percent of full scale. The temperature drift is $\pm$ 0.02 percent of full scale per Kelvin.

Power Metering

The power fed to the evaporator is measured by a power transducer (Hartmann & Braun, ETP 35) giving linear, analog DC–output signals between 0 - 20 mA, 20 mA corresponding to full scale. The uncertainty of the transducer is $\pm$ 0.5 percent of full scale. The power is indicated by a moving – coil ammeter (measuring range 0 - 20 mA, uncertainty, 1 percent of full scale).
The test section is heated electrically by direct current. The power input is determined by measuring the current with a shunt ($R = 20 \cdot 10^{-6}\Omega$) and the voltage over the tube. Uncertainties correspond to the accuracy of the voltmeter (HP 3456,A).

Liquid Temperature, Saturation Temperature

Liquid temperatures are measured in the orifice section for determination of liquid density and at the evaporator inlet. Saturation temperature is measured at the evaporator outlet. At each measuring point 20 temperature measurements were taken and averaged in order to equalize random temperature fluctuations. The estimated uncertainties of liquid temperature and saturation temperature are expected to be ± 0.3 K.

Wall Temperatures

Wall temperatures are measured on the outer side of the tube by cromel–alumel thermocouples (0.5 in diameter), which are distributed over the tube length and circumference, as scetched in fig. 2. The wall temperatures at the inner side are calculated with Fourier differential equation for steady state, one dimensional heat conduction with inner heat source.

$$\frac{d^2T}{dr^2} + \frac{1}{r} \cdot \frac{dT}{dr} + \frac{\dot{w}}{\lambda} = 0 \tag{2}$$

Integration of equation (2) yields

$$T_i = T_o - \frac{\dot{q} R_i}{\lambda} \left[\frac{R_o^2}{R_o^2 - R_i^2} ln \frac{R_o}{R_i} - \frac{1}{2} \right]$$

$\dot{w}$ = *volumetric power input* $[W/m^3]$

λ = *thermal conductivity* $[W/mK]$

$R_{i,o}$ = *inner and outer radius of tube, respectively* $[m]$

$\dot{q}$ = *heat flux density* $[W/m^2]$

$T_{i,o}$ = *wall temperatures at the inner and outer side, respectively* $[m]$

r = *radial distance* $[m]$

As mentioned above, differences in wall thickness are small, so variability of conduction could be neglected. Heat losses of the test section, determined depending on wall temperature, are small compared with power input (< 1 %).

Vapour Temperatures

The vapour temperature is measured in two different ways. On one hand a vapour probe is used which utilizes inertial separation of liquid droplets from vapour. It consists of two small concentric tubes and a thermocouple in the centre. The sampled fluid, which is sucked off from the flow, has to undergo a 180° change in direction before streaming into the inner tube and passing over the thermocouple. This directional change provides the

inertial separation of liquid from vapour. Droplets impacting on the bottom of the probe and forming a liquid film are sucked off before reaching the top access hole (figure 4).
On the other hand, we used three bare thermocouples (chromel–alumel, 0.5 mm in diameter), that is to say, the thermocouples are not shielded from impacting droplets. They are mounted perpendicular to the flow direction before and after the bend.
Both the vapour probe and the bare thermocouples are movable across the tube, which has two considerable advantages. The first one is that local measurements of the vapour temperature can be made, the second one is that the probes can be pulled out of the flow channel and the wall temperatures can be recorded at flow conditions being not disturbed.

Droplet Concentration

Right after the bend outlet a so called impedance–void–meter is installed. This device is provided for measuring the droplet concentration in different areas of the cross section. It consists of four concentric tubes, one of them subdivided in four parts, and a cylindrical pin in the centre, which are wired to five separate capacitors (figure 5 and 6). They are supplied with a high frequency voltage (1 MHz).
Generally, the impedance method is based on the difference between liquid and vapour electrical conductivity and dielectric constant. In our case the impedance of the two phases mixture only depends on the dielectric constant because the test fluid (refrigerent R 12) has a negligibly low conductivity.
Depending on the flow pattern the void fraction can be calculated as a function of the total dielectric constant of the two–phase flow. In the post dryout region the flow pattern corresponds to small liquid droplets dispersed in a vapour bulk. It is assumed that this flow pattern exists up to the end of the curved tube where the capacitive sensor is installed and the void fraction is calculated by means of the Maxwell–equation:

$$1 - \epsilon = \frac{e - e_v}{e - 2e_v} \cdot \frac{e_l + 2e_v}{e_l + e_v} \tag{3}$$

e_v = *dielectric constant of saturated vapour*
e_l = *dielectric constant of saturated liquid*
e = *dielectric constant of two phase mixture*
ϵ = *void fraction*

e_v and e_l are known from literature, e is determined from the capacity C_M

$$C_M = eC_0 + C_p \tag{4}$$

which is measured with a precision capacity meter (BOONTON ELECTR. CO, Typ 72BD). The quantities C_0 only depend on geometry of the void meter, and C_p due to parasitic capacity are assumed to be constant. They are determined by two capacity measurements at conditions where e is well known. On one hand vacuum was chosen (e =

1.0), on the other hand pure liquid condition was taken where e is known from literature. If C_0 and C_p are determined in this way e can be easily evaluated from equation (4).

A detailed description of experimental apparatus can be found in | 1 |.

Data Acquisition

Test loop measurements and controls were accomplished using a computer (HP 3495, A) and a digital voltmeter (HP 3456, A). Measurements and loop parameters were displayed continuously on a terminal, allowing monitoring by an operator.
All measuring data were recorded at a rate of 10 data/sec. From the differential pressure across the orifice, the absolute pressure, the voltage and the current of the test section 20 measurements were taken and averaged, respectively in order to avoid random fluctuations.

3. Experimental Results

Post dryout experiments were carried out systematically at various parameters shown in the following tabulation.

mass flow rate (kg/m^2s)	$\dot{m}$	:	400, 680, 1240, 2000
heat flux density (kW/m^2)	$\dot{q}$	:	20, 30, 40, 50, 60, 70
pressure (bar)	p	:	9.5, 19.1, 28.5, 38.0
corresponding pressure ratio	p/p_{crit}	:	0.23, 0.46, 0.70, 0.93
diameter of curvature (m)	D_C	:	0.200, 0.400, 0.610
corresponding diameter ratio	D_c/D	:	14, 28, 42
length of curvature $(degree)$	L_c	:	90, 450

These parameters were restricted by film boiling in the straight test section and by wall temperatures over 250°C . In order to investigate the influence of various parameters upon heat transfer – for instance the reduced pressure ratio – only this parameter was varied in the experiments and the other ones – in our example mass flow rate, heat flux density and position of the dryout point – were kept constant. In the following some experimental data are presented for the straight and curved tube, respectively.

3.1. Straight Tube

3.1.1. Dryout Quality

The quality at the dryout point was calculated by means of an energy balance.

$$\dot{x}_{DO} = \frac{1}{h_{fg}\dot{m}} \left[\dot{Q}_{ev} + \dot{Q}_{D0} - \dot{Q}_{hl} - \dot{m}(h_{l,S} - h_{l,e})\right] \tag{5}$$

$\dot{Q}_{ev}$ = *power fed to evaporator* $[W]$

$\dot{Q}_{D0}$ = *power fed to test section up to dryout* $[W]$

$\dot{Q}_{hl}$ = *heat losses up to dryout* $[W]$

$h_{l,S}$ = *enthalpy of saturated liquid* $[kJ/kgK]$

$h_{l,e}$ = *enthalpy of subcooled liquid before evaporator* $[kJ/kgK]$

h_{fg} = *heat of evaporation* $[kJ/kg]$

$\dot{m}$ = *total mass flow rate* $[kg/s]$

The influence of pressure ratio, heat flux density and mass flow rate upon the dryout quality is illustrated in figure 7 and 8. The corresponding data are listed in table 1 and 2. An increase in head flux density leads to enhanced evaporation associated with larger entrainment rates and lower dryout qualities. Higher mass flow rates are associated with higher velocity of flow, larger momentum transfer between vapour and liquid phase and consequently with enhanced entrainment. Therefore dryout quality decreases with increasing mass flow rates. Rising pressure results in an increase in density and in viscosity of vapour phase and in a decrease of surface tension of liquid phase. Thereby entrainment is also improved and dryout occurs at lower qualities.

3.1.2. Wall Temperature

Wall temperature curves at four different mass flow rates are shown in figure 9. As can be seen higher mass flow rates induce a smaller temperature rise at the dryout point and better heat transfer in the post dryout region. This is mainly due to higher vapour velocity, which can be explained in heat transfer correlations by a higher Reynolds – number.

The influence of heat flux density upon heat transfer is illustrated in figure 10. Higher wall heat flux produces an increase in wall temperature as well at the dryout as in the post dryout region. The gradients of the temperature curves slightly decrease with rising heat flux. This can be explained by higher vapour temperatures which result in an enhanced droplet evaporation, in an increase in vapour velocity and, consequently, in a better heat transfer coefficient.

Wall temperature curves at different pressure ratios are hardly to compare, because the saturation temperature and the whole temperature level increase with pressure. Therefore, in figur 11 the temperature differences between the wall temperature and the corresponding saturation temperature are plotted versus the length of the tube. Figure 11 shows that the influence of pressure upon the temperature rise at the dryout point is small, however, in the post dryout region it is considerable. While the wall temperatures increase at low pressure they decrease at high pressure.

Different pressures do not only influence thermodynamic properties, but also flow conditions like quality, velocity of flow, drop size etc. Therefore, it is difficult to predict how heat transfer is affected. An increase in pressure leads to a lower Reynolds – number of vapour phase, due to lower velocity and larger viscosity of vapour phase. On the other hand

the Prandel – number Pr and the conductivity λ of vapour increase. The heat transfer coefficient h in the post dryout region is a function of these quantities

$$h \sim f(Re, Pr, \lambda)$$

and is affected only a little by different pressures.
A more important reason for better heat transfer at high pressures seems to be a smaller extend of thermodynamic nonequilibrium. Due to lower droplet velocity the period of residence within an axial distance increases and so does the quantity of heat transfered to the droplets. In addition the droplet evaporation is intensified by a lower heat of evaporation leading to lower vapour temperatures. This is confirmed by measurements of the vapour temperature which will be discussed in the following.

3.1.3. Superheating of Vapour

In order to receive information on thermodynamic nonequilibrium the vapour temperature was determined at a distance of 2.35 m ($L/D = 82$) downstream of the dryout by the vapour probe described in chapter two. The vapour temperature was measured in the core of the flow and at equal distances of 4 mm towards the tube wall.
At each position 60 temperature data were recorded within a period of about 10 seconds. A typical curve of the measured temperature is shown in figure 12. The decrease and increase in temperature is due to wetting and drying out of the thermocouple. The vapour temperature can be obtained from the maxima of the curve.
Considerable superheatings of vapour were only observed at low mass flow rates, high wall heat flux and low pressure. The influence of these parameters can be seen in figure 13 to 15, where the difference between vapour and saturation temperature is plotted versus the distance from the tube wall. The corresponding data are listed in table 6 to 8. The diagrams show that the vapour temperature is almost constant in the core of the flow and rises close to the wall. An increase in mass flow rate and pressure lead to smaller, an increase in heat flux density to larger superheatings of vapour.

3.2. Curved Tubes

A precise description of the flow in a curved tube is very difficult due to a secondary flow superimposing on the main flow and even for a single phase fluid the details are not yet known completely. Therefore, post – dryout heat transfer in curved tubes is not only a problem of thermodynamic nonequilibrium but also of very complicated fluiddynamic processes. The main differences in dispersed flow between straight and bent tubes are the following:
In a curved tube, the fluid in the core is driven towards the outer side by centrifugal force. This process produces a pressure gradient across the tube assuming its maximum value at the outer side. As the pressure force prevails near the wall the fluid streams along the wall

surface to the inner side of the bend. Thus, the secondary flow forms a pair of vortices in the cross section, as sketched in figure 16.
The profile of vapour velocity changes along the bend. Beginning with an acceleration of the flow at the inner side the maximum of velocity moves towards the outer side due to the secondary flow.
The slip ratio and the interfacial heat transfer between the phases increase, as the droplets entering the bend move faster towards the outer side than the vapour.
Due to a higher radial droplet velocity, the number of droplets impacting on the outer bend wall increases and in case of low wall heat flux rewetting is possible. Whereas droplet – wall contacts are usually neglected in straight tubes, they are of great importance in heat transfer in bent tubes.
In curved tubes the droplet concentration in the cross section is inhomogeneous due to a centrifugal force. Consequently, the extent to which the vapour is superheated depends on the position in the cross section.

In the following it will be shown by some examples how post dryout heat transfer is influenced by different test conditions.
In this paper the far side of the wall from the axis of curvature is called the outer wall, and the near side is called the inner wall.

3.2.1. Wall Temperature

Wall temperature curves of the inner and outer side of the bend are shown in figure 17. The wall temperatures are plotted versus the axial position of the bend, 0 and 90 degree correspond to the bend inlet and outlet, respectively.
As can be seen, at first heat transfer is improved at the outer wall, due to an increase in droplet concentration and in vapour velocity and rewetting occurs at a bend angle of 20 degree. At the inner side the wall temperatures increase up to a bend angle of 15 degree. Downstream, heat transfer is improved, too, due to a secondary flow bringing coolant from the outer side and after a distance even rewetting of the inner wall occurs.

Increasing wall heat flux leads to higher wall temperatures in the straight and in the curved tube. Above a particular heat flux density, which depends on mass flow rate, pressure ratio and diameter of curvature, rewetting of the outer wall is no longer able (figure 18).

The ability to rewet the outer wall also decreases with rising pressure. As is illustrated in figure 19, at low pressure rewetting is possible despite of high superheating of the wall, whereas at high pressure and even lower wall heat flux rewetting does not occur.
Whether a drop impacts on the wall or not mainly depends – beside the wall temperature – on droplet velocity perpendicular to the wall (= droplet deposition velocity) and on reaction force which is due to nonuniform droplet evaporation. An increase in pressure leads to smaller droplet deposition velocity. On one hand this is due to a stronger droplet deflection by vapour flow due to higher density ratio ρ_v/ρ_l, on the other hand it is due to the lower flow velocity mentioned above. Close to the hot wall the mass of vapour

generated on the drop side facing the wall is larger than that generated on the opposite side. As a consequence the drop is pushed away from the wall. Owing to smaller heat of evaporation this reaction force increases with pressure.
The influence of mass flow rate upon heat transfer in curved tubes is shown in figure 20, where wall temperatures are plotted versus the tube angel (= angel in circumferential direction) at different axial positions. Tube angles of 0 and 180 degree correspond to the outer and inner side of the bend, respectively. Figure 20a shows temperature curves at a low and figure 20b at a high mass flow rate. It is well known from straight tubes that an increase in mass flow rates induces better heat transfer in the post dryout region and, consequently, lower wall temperatures at the bend inlet.
Fig. 20 also illustrates that the axial wall temperature gradient all over the circumference is considerably lower at high mass flow rate. Partially this is due to lower superheating of the wall and lower vapour temperature which results in less vigorous evaporation of droplets. But there must be another effect, as the wall temperatures at high mass flow rate can even exceed those at low mass flow rate at the bend outlet.
Decreasing wall temperatures are due to the secondary flow bringing coolant from the outer side. Steep temperature decreases, as can be seen in figure 20a all over the circumference, indicate strong additional cooling of the wall by droplets. With increasing mass flow rate both the velocity of primary and secondary flow rise. Obviously, as the small temperature decreases in fig. 20b show, the velocity of primary flow increases faster than that of the secondary flow. Thus the vapour and mainly the droplets cover shorter circumferential distances on their helical path through the bend and the additional secondary cooling of the wall decreases.

3.2.2. Superheating of Vapour

The distribution of vapour temperature in a bend is very difficult to predict. It depends on the distribution of droplet concentration, on the slip ratio between the two phases, and on the velocity profile of the developing vapour flow, which all change along the bend.
Right after the bend outlet the vapour temperature was measured by two bare thermocouples, which are movable across the tube. Fig. 21 shows different vapour temperature profiles which were detected.
At low heat flux density and low mass flow rate the highest superheating of vapour was measured in the core of the flow. At first sight this result seems to be strange. In this case vapour superheated at the inner wall and slowly driven toward the outer side was enclosed by droplets and by vapour cooled down at the outer wall, which streamed along the circumference up to the inner wall.
With increasing heat flux densities the drop evaporation at the outer wall and along the circumference is intensified and the vapour moving inward is cooled less. Thus the superheating of vapour increases from the outer to the inner wall.
If the same measurements are carried out at higher mass flow rate, a temperature maximum in the core of the flow, as shown in fig. 21, cannot be detected. Though the liquid fraction

is higher in these experiments, the vapour temperatures increase continuously from the outer to the inner wall. This is due to a smaller velocity ratio of the secondary to the main flow.

3.2.3. Droplet Concentration

The distribution of droplet concentration in the cross section mainly depends on the centrifugal forces, which vary with mass flow rate and pressure ratio. In the experiments carried out the flow velocity is usually so high that buoyancy force and gravity can be neglected. Only at very high pressure and low mass flow rate gravity gains more importance.
The void fraction was measured right after the bend outlet by the impedance – void – meter, described in chapter 2. Though the void fraction is very high at this position, considerable differences in droplet concentration could be detected in different areas of the cross section.
In the example shown in figure 22, close to the inner wall (3) there is nearly pure vapour flow. In the core of the flow (2) the liquid fraction is a little higher, but low compared with the outer region (1) in which the predominant part of the droplets flows.
In figure 23 time averaged void fractions are plotted versus the heat flux density. From wall temperatures it is known that in these experiments rewetting of the outer wall occured up to 40 kW/m^2. This results in strong droplet evaporation and high void fraction close to the outer wall. As soon as rewetting ceases (from 50 kW/m^2 on) the evaporation decreases considerably and so does the void fraction close to the outer wall, as can be seen in figure 23. In case of no rewetting it was also observed that the void fraction close to the inner wall increases (fig. 23). This indicates that the inward droplet flow decreases, due to less penetration of droplets in the boundary layer where the secondary flow takes place.
A detailed description of dispersed flow heat transfer in curved tubes and modelling of heat transfer con be found in | 1 | and | 2 |.

References

| 1 | Lautenschlager G.
Wärmeübergang in Krümmern bei Sprühkühlung,
Dissertation, Technische Universität München, 1988

| 2 | Lautenschlager G, Mayinger F.
Experimental Investigation of Dispersed Flow Heat Transfer in Curved Tubes;
International Symposium on Phase Change Heat Transfer, Chongqing University,
Chongqing, P. R. China, May 20.–23., 1988

Table 1

Influence of heat flux density $\dot{q}$ and pressure p upon dryout quality $\dot{x}_{DO}$

$\dot{x}_{DO}$	$\dot{q}(kW/m^2)$	$\dot{m}(kg/m^2s)$	$p(bar)$
0.762	20.5	1242	9.5
0.697	30.0	1246	9.5
0.606	40.7	1240	9,5
0.561	50.2	1249	9.5
0.496	60.1	1246	9.5
0.447	70.3	1239	9.5
0.532	20.1	1256	19.1
0.474	30.0	1243	19.1
0.413	40.7	1246	19.1
0.357	50.1	1246	19.1
0.328	60.4	1243	19.1
0.295	70.4	1237	19.1
0.472	20.2	1237	28.5
0.414	30.3	1239	28.5
0.353	40.5	1237	28.5
0.309	50.1	1240	28.5
0.241	60.5	1236	28.5
0.192	70.1	1245	28.5

Table 2

Influence of mass flow rate $\dot{m}$ ~~and pressure p~~ upon dryout quality $\dot{x}_{DO}$

$\dot{x}_{DO}$	$\dot{m}(kg/m^2s)$	$\dot{q}(kW/m^2)$	$p(bar)$
0.754	407	40.0	9.5
0.664	683	40.5	9.5
0.606	1240	40.7	9.5
0.558	2005	41.5	9.5
0.727	405	50.3	9.5
0.611	688	50.2	9.5
0.561	1249	50.2	9.5
0.544	2007	51.0	9.5

Table 3

Influence of mass flow rate $\dot{m}$ upon heat transfer

$p(bar)$	19.1	19.1	19.1	19.1
$\dot{q}(kW/m^2)$	40.27	40.39	40.68	40.32
$\dot{m}(kg/m^2s)$	400.4	678.0	1245.7	2000.2
$L(cm)$		$T_{Wall}(°C)$		
86.6	76.2	77.0	76.2	75.0
96.6	99.2	123.9	92.0	97.7
106.6	162.5	148.5	120.0	103.5
116.6	169.7	151.5	128.5	106.0
166.6	180.8	158.3	135.8	106.3
226.6	176.4	151.7	130.3	103.0
286.6	182.6	152.4	129.6	102.7
296.5	181.5	151.9	129.8	102.4
306.6	183.7	154.0	132.2	103.7
336.6	180.6	148.7	125.7	100.2

Table 4

Influence of heat flux density $\dot{q}$ upon heat transfer

$p(bar)$	19.1	19.1	19.1
$\dot{m}(kg/m^2s)$	685.1	681.3	680.6
$\dot{q}(kW/m^2)$	30.27	50.35	69.92
$L(cm)$		$T_{Wall}(°C)$	
86.6	79.5	76.5	76.9
96.6	116.1	152.6	137.7
106.6	125.6	169.4	225.4
116.6	127.7	174.6	232.8
166.6	133.5	181.8	236.8
226.6	129.2	172.8	221.6
286.6	130.2	172.4	218.0
296.6	130.2	171.7	216.6
306.6	132.1	174.1	218.7
336.6	127.8	167.6	210.0

Table 5

Influence of pressure p upon heat transfer

$\dot{q}(kW/m^2)$	40.5	40.39	40.33
$\dot{m}(kg/m^2s)$	682.5	678.0	678.2
$p(bar)$	9.5	19.1	28.5
$L(cm)$	T_{Wall}	$-T_{Sat}(°C)$	
86.6	8.0	5.9	2.4
96.6	52.4	52.7	30.5
106.6	78.5	77.3	66.9
116.6	84.2	80.4	69.2
166.6	96.3	87.2	70.7
226.6	97.6	80.6	62.1
286.6	102.2	81.3	62.4
296.6	102.8	80.8	62.0
306.6	102.6	82.9	64.2
336.6	101.2	77.6	59.1

Table 6

Influence of pressure p upon superheating of vapour

$\dot{q}(kW/m^2)$	50.32	50.49	50.15
$\dot{m}(kg/m^2s)$	404.6	399.0	403.6
$p(bar)$	9.5	19.1	28.5
$r(mm)$	T_V	$-T_{Sat}(°C)$	
2.5	43.5	38.6	23.8
6.5	30.1	17.6	8.9
10.5	26.3	16.5	5.0
14.5	27.8	14.4	8.2

Table 7

Influence of mass flow rate $\dot{m}$ upon superheating of vapour

$p(bar)$	9.5	9.5	9.5
$\dot{q}(kW/m^2)$	50.32	50.16	70.15
$\dot{m}(kg/m^2s)$	404.6	687.5	1248.7
$r(mm)$	T_V	$-T_{Sat}(°C)$	
2.5	43.5	22.1	12.2
6.5	30.1	18.0	4.7
10.5	26.3	15.8	5.1
14.5	27.8	15.7	2.9

Table 8

Influence of heat flux densitie $\dot{q}$ upon superheating of vapour

$p(bar)$	9.5	9.5
$\dot{m}(kg/m^2s)$	400.6	404.6
$\dot{q}(kW/m^2)$	30.08	50.32
$r(mm)$	T_V	$-T_{Sat}(°C)$
2.5	13.9	43.5
6.5	9.8	30.1
10.5	13.0	26.3
14.5	11.3	27.8

Table 9

Wall temperatures at the outer and inner side of the bend

$\dot{m} = 682.5\ kg/m^2s$ $p = 9.5\ bar$ $\dot{q} = 40.50\ kW/m^2$ $D_c/D = 42$		
	$T_{Wall}(°C)$	
bend angle (deg)	outer side	inner side
before inlet	139.1	142.7
0	130.6	143.7
10	104.5	150.5
15	101.8	153.0
20	44.9	151.4
30	44.6	144.9
45	43.3	133.1
60	43.7	67.7
75	44.1	46.6
90	45.1	46.9

Table 10

Influence of heat flux density upon heat transfer at the outer wall of a bend ($D_c/D = 42$)

$p(bar)$	9.5	9.5	9.5
$\dot{m}(kg/m^2s)$	686.8	687.5	680.7
$\dot{q}(kW/m^2)$	29.64	50.16	70.00
bend angle (deg)	$T_{Wall}(°C)$		
before inlet	107.8	162.8	225.9
0	102.1	151.3	207.6
5	61.1	130.0	182.7
10	43.3	119.8	170.5
15	43.4	116.4	163.5
20	43.3	110.1	154.6
30	43.0	111.9	154.0
45	42.5	118.5	164.0
60	42.8	120.4	167.6
75	42.8	120.8	169.4
90	43.2	122.1	172.1

Table 11

Influence of pressure upon heat transfer at the outer wall of a bend ($D_c/D = 42$)

$\dot{m}(kg/m^2s)$	1245.9	1245.7
$\dot{q}(kW/m^2)$	60.05	40.68
$p(bar)$	9.5	19.1
bend angle (deg)	T_{Wall}	$-T_{Sat}(°C)$
before inlet	97.6	56.4
0	80.8	49.2
5	28.5	44.1
10	4.7	39.3
15	4.7	38.2
20	4.9	38.0
30	4.6	37.6
45	3.5	37.2
60	3.9	37.2
75	4.5	40.5
90	4.0	40.1

Table 12

Influence of mass flow rate upon heat transfer in a bend

$p = 9.5\ bar$
$\dot{q} = 41.67\ kW/m^2$
$\dot{m} = 687.1\ kg/m^2 s$
$D_c/D = 14$

	T_{Wall} $(°C)$						
	tube	angle	(deg)				
bend angle (deg)	0	30	60	90	120	150	180
15	43.4	42.7	63.3	100.7	132.7	147.0	152.2
45	43.6	43.2	52.2	87.2	112.2	127.2	136.8
75	42.2	42.6	44.1	47.1	58.3	93.2	107.6
90	42.6	42.6	42.2	44.6	45.0	50.1	59.5

$p = 9.5\ bar$
$\dot{q} = 42.47\ kW/m^2$
$\dot{m} = 1991.6\ kg/m^2 s$
$D_c/D = 14$

	T_{Wall} $(°C)$						
	tube	angle	(deg)				
bend angle (deg)	0	30	60	90	120	150	180
15	40.4	39.8	42.3	54.0	73.5	82.7	85.7
45	41.3	40.4	42.1	52.4	67.0	75.4	80.8
75	40.3	40.7	42.5	56.6	68.8	77.2	82.5
90	41.3	41.2	41.7	46.6	64.7	75.0	79.6

Table 13

Distribution of vapour temperature after the bend outlet

$p\ (bar)$	9.5	9.5	9.5
$\dot{m}\ (kg/m^2s)$	683.7	678.6	681.0
$\dot{q}\ (kW/m^2)$	31.17	50.10	71.17
$D_c/D = 14$			
radial position	T_{Vapour}	$(°C)$	
-12	39.4	79.3	142.0
-8	43.3	78.7	113.8
-4	50.8	79.6	107.7
0	56.7	75.4	94.7
4	51.5	60.4	72.5
8	40.0	44.3	50.0
12	39.4	42.4	39.7

Table 14

Void fraction close to the outer and inner wall after the bend outlet

$\dot{q}\ (kW/m^2)$	$p\ (bar)$	$\dot{m}\ (kg/m^2s)$	$\epsilon\ (o.s.)$	$\epsilon\ (i.s.)$
20.50	9.5	686.3	0.949	0.971
29.64	9.3	686.8	0.944	0.975
40.50	9.5	682.5	0.943	0.978
50.16	9.5	687.5	0.857	0.999
59.93	9.5	679.0	0.850	1.000
70.00	9.5	680.7	0.831	1.000

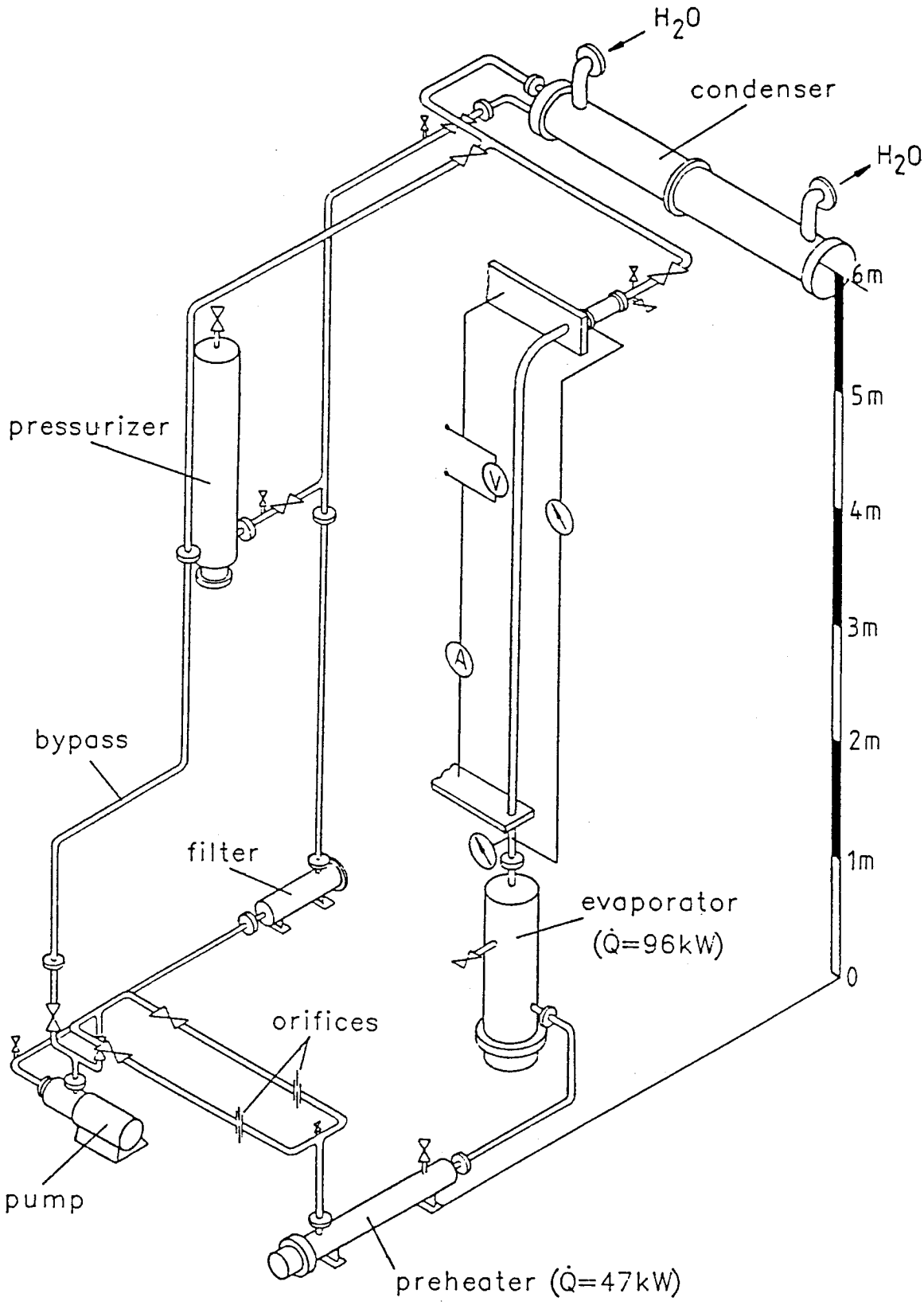

Fig. 1: Test loop

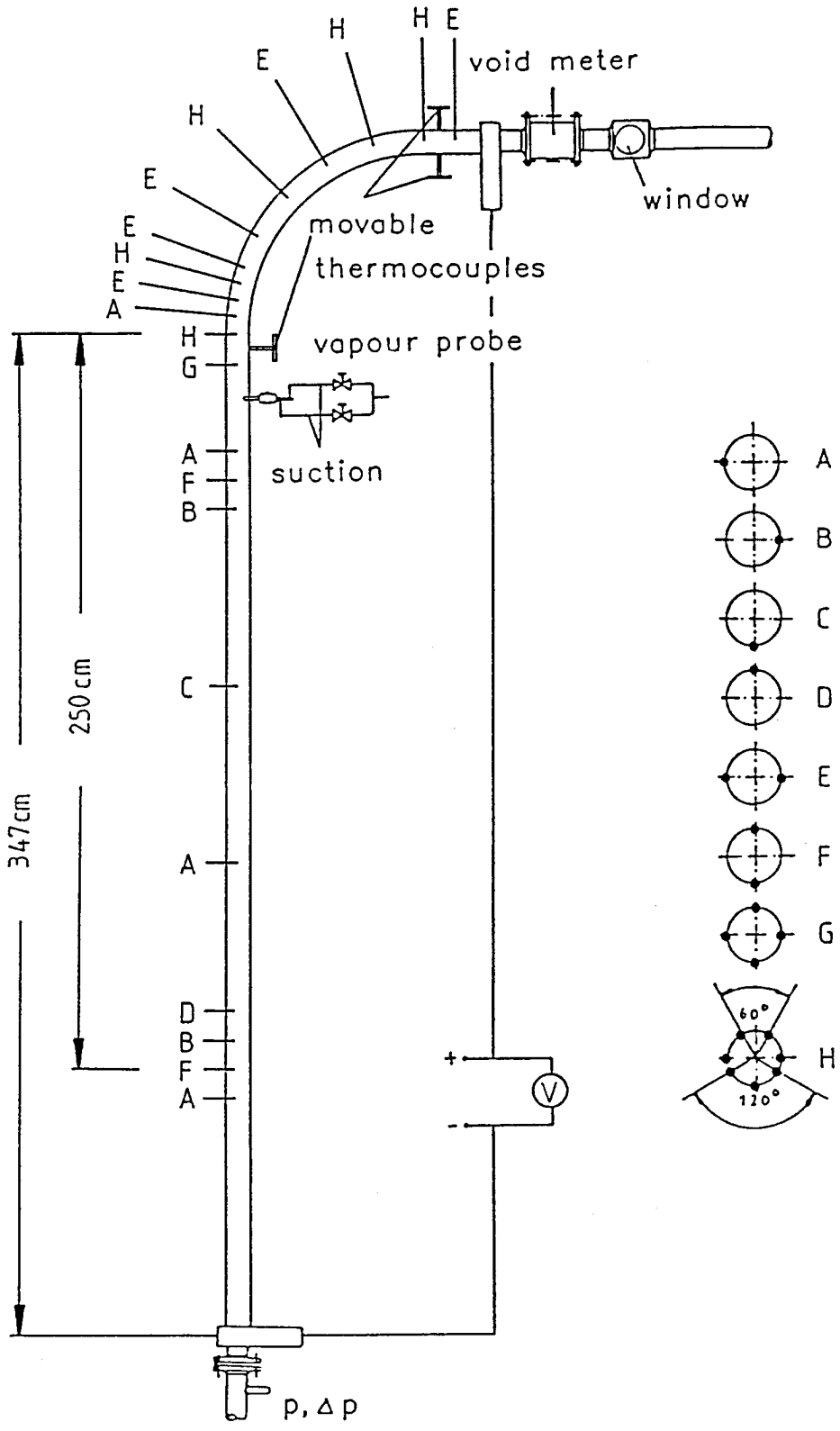

Fig. 2: Test section and distribution of thermocouples

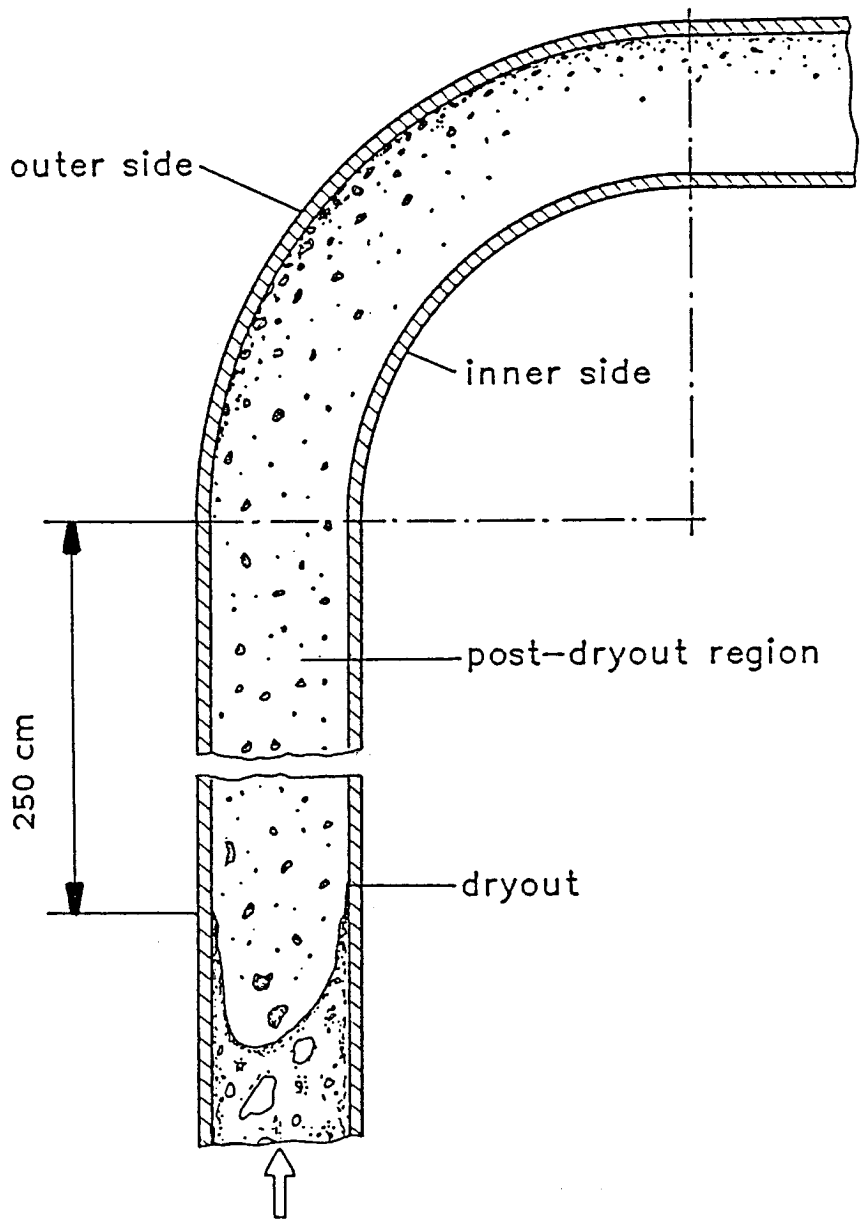

Fig. 3: Dispersed flow in straight and curved tubes

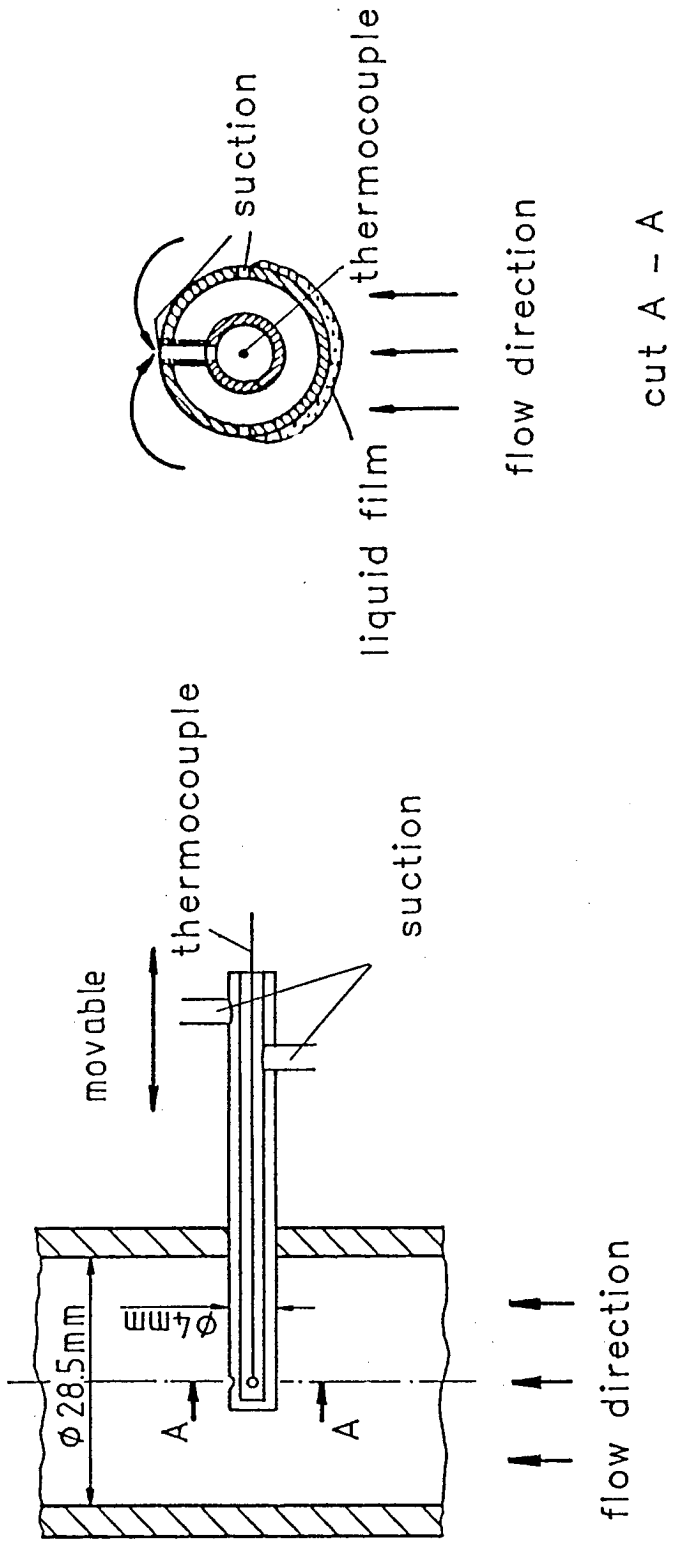

Fig. 4: Vapour probe

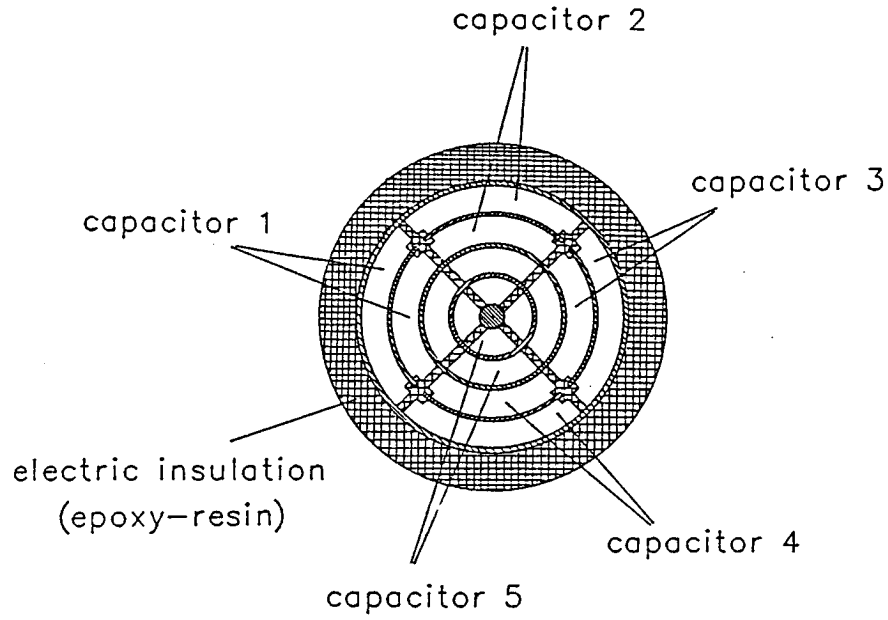

Fig. 5: Impedance–void–meter

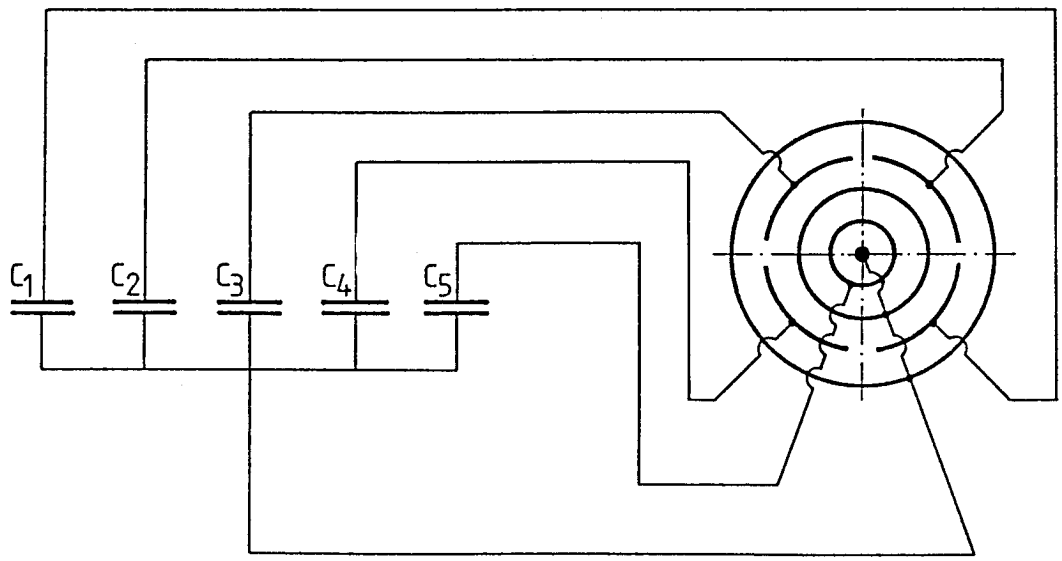

Fig. 6: Wiring of capacitors

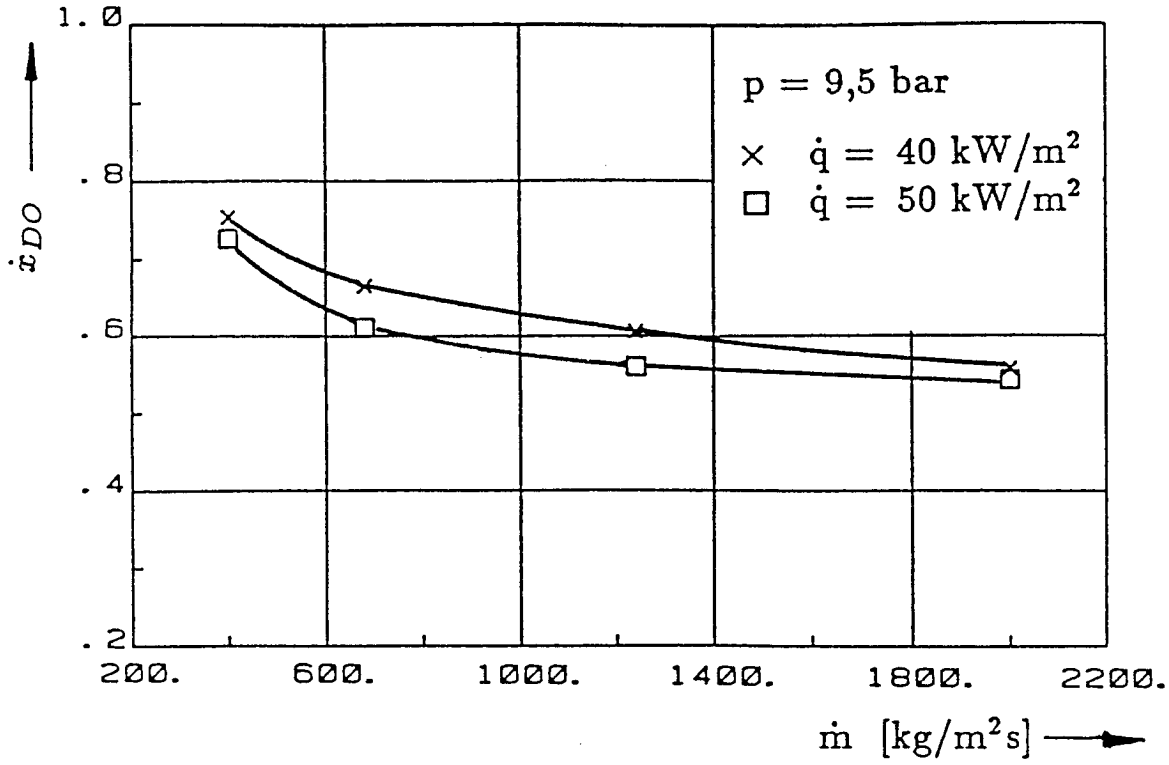

Fig. 7: Influence of mass flow rate upon dryout quality

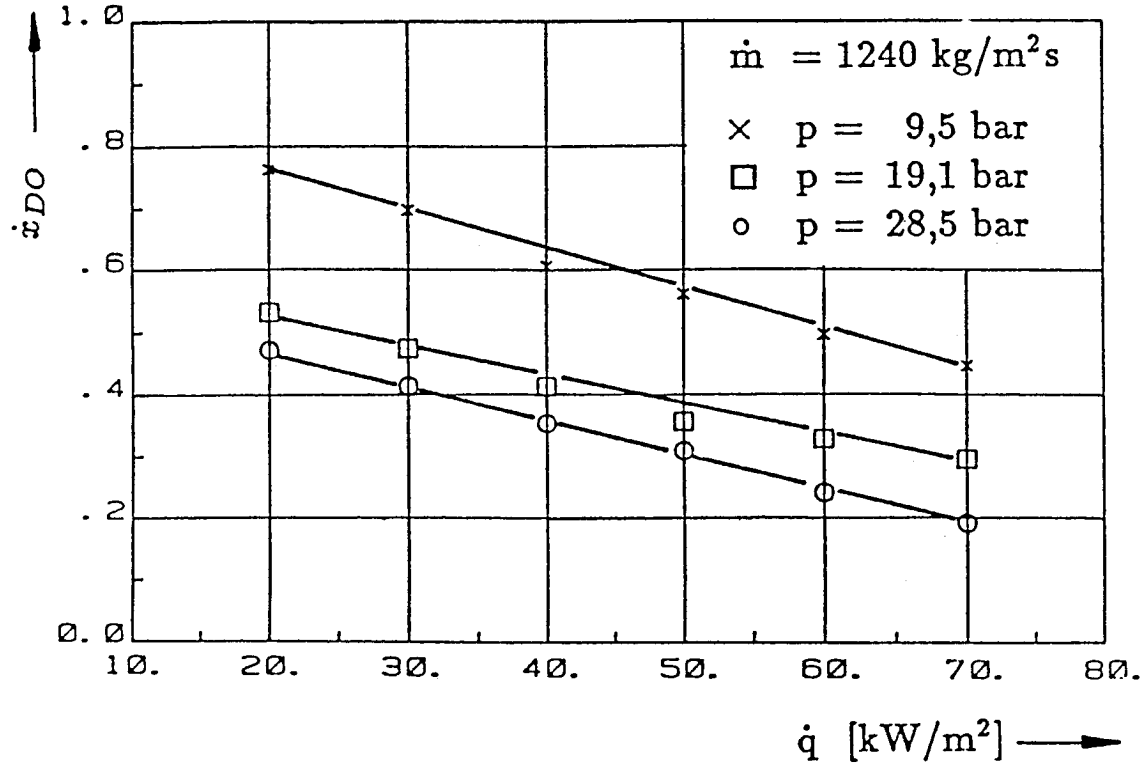

Fig. 8: Influence of pressure and heat flux density upon dryout quality

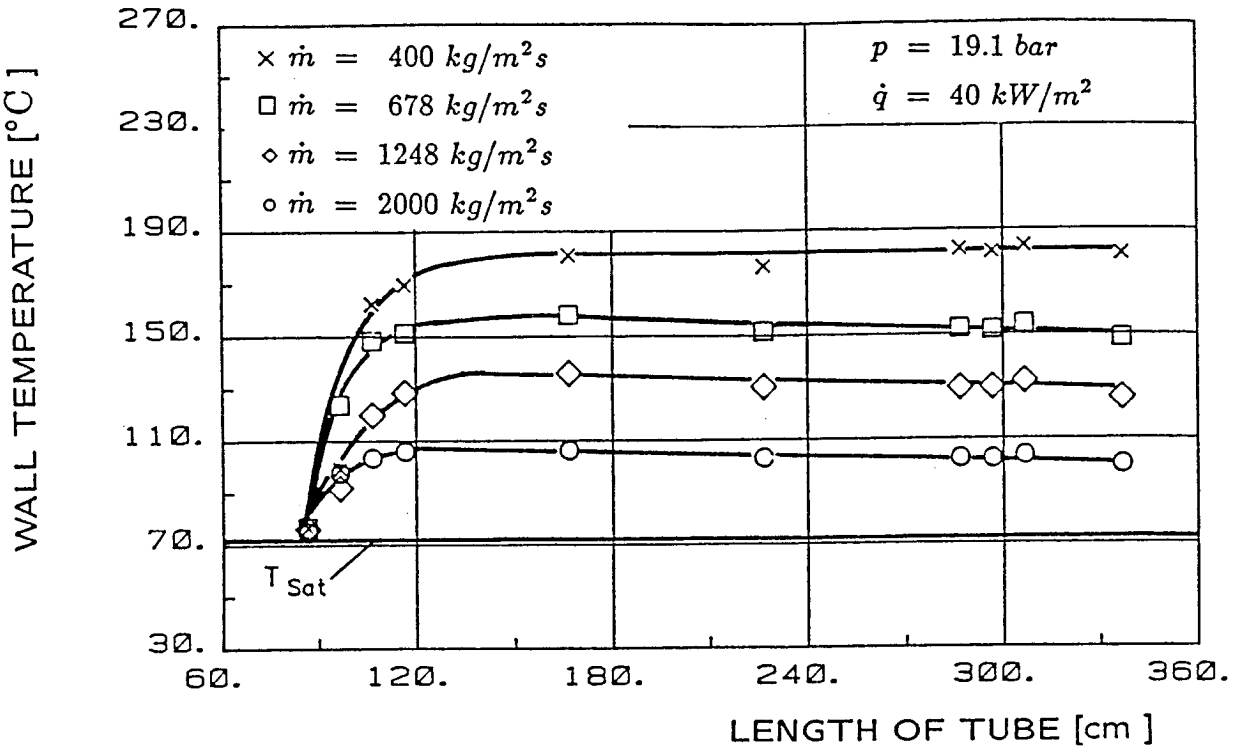

Fig. 9: Influence of mass flow rate upon heat transfer

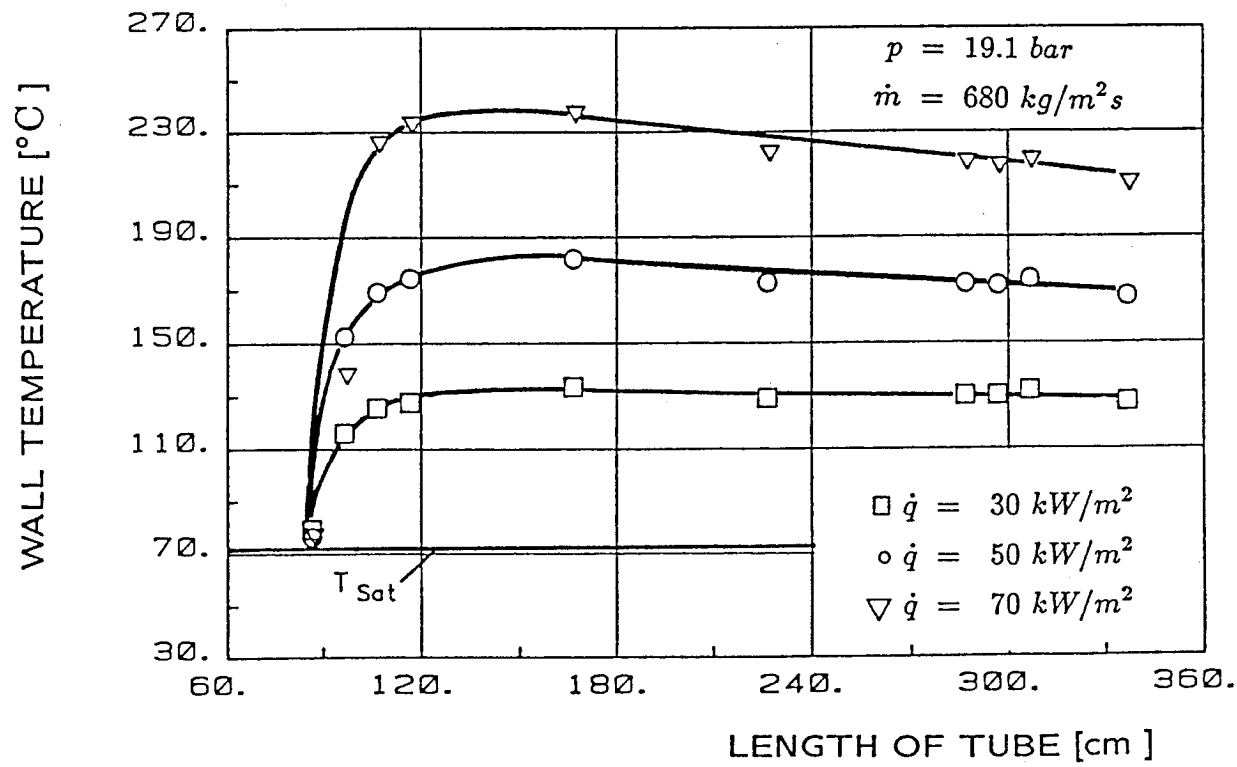

Fig. 10: Influence of heat flux density upon heat transfer

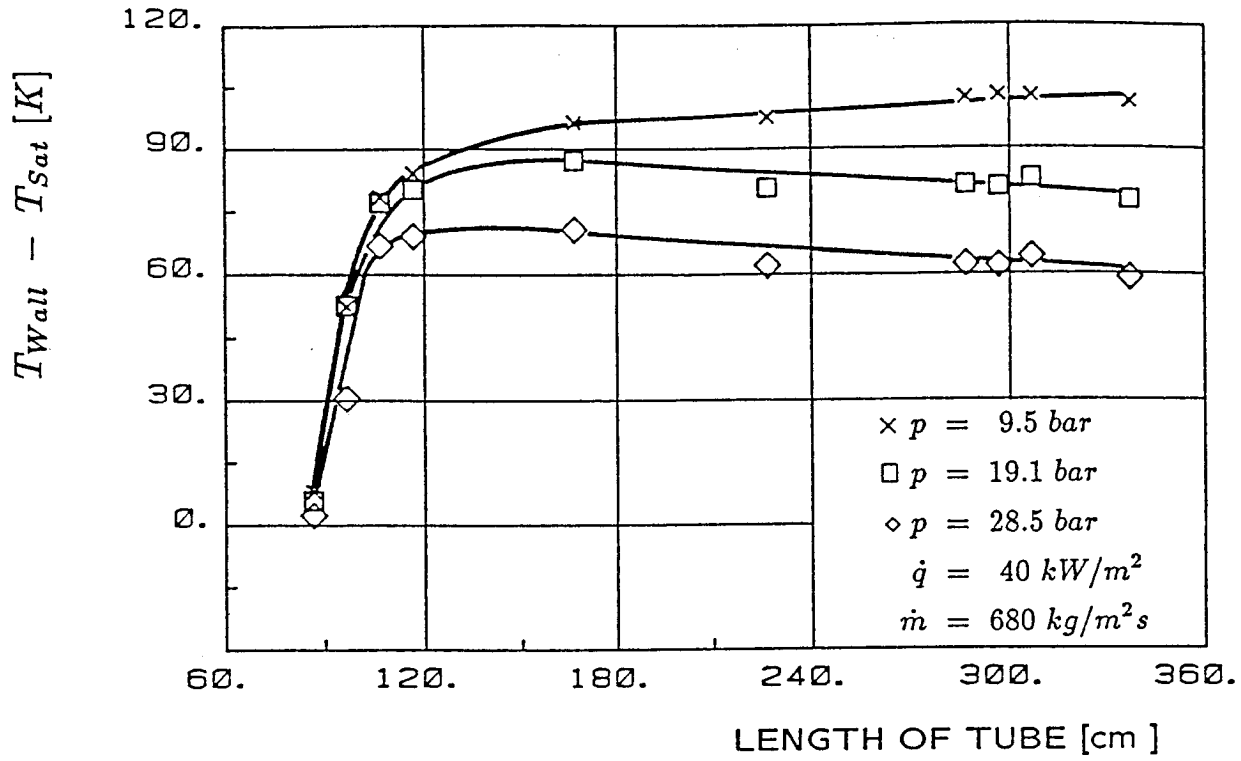

Fig. 11: Influence of pressure upon heat transfer

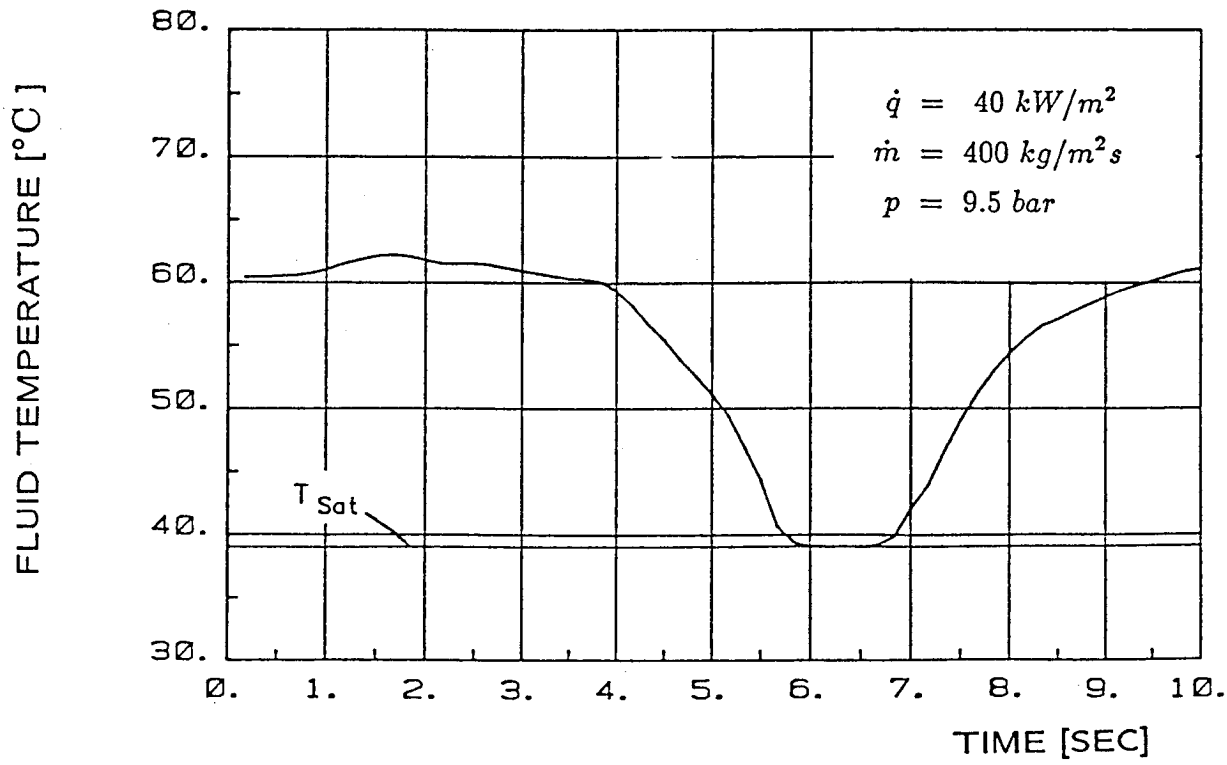

Fig. 12: Vapour temperature measured by the vapour probe

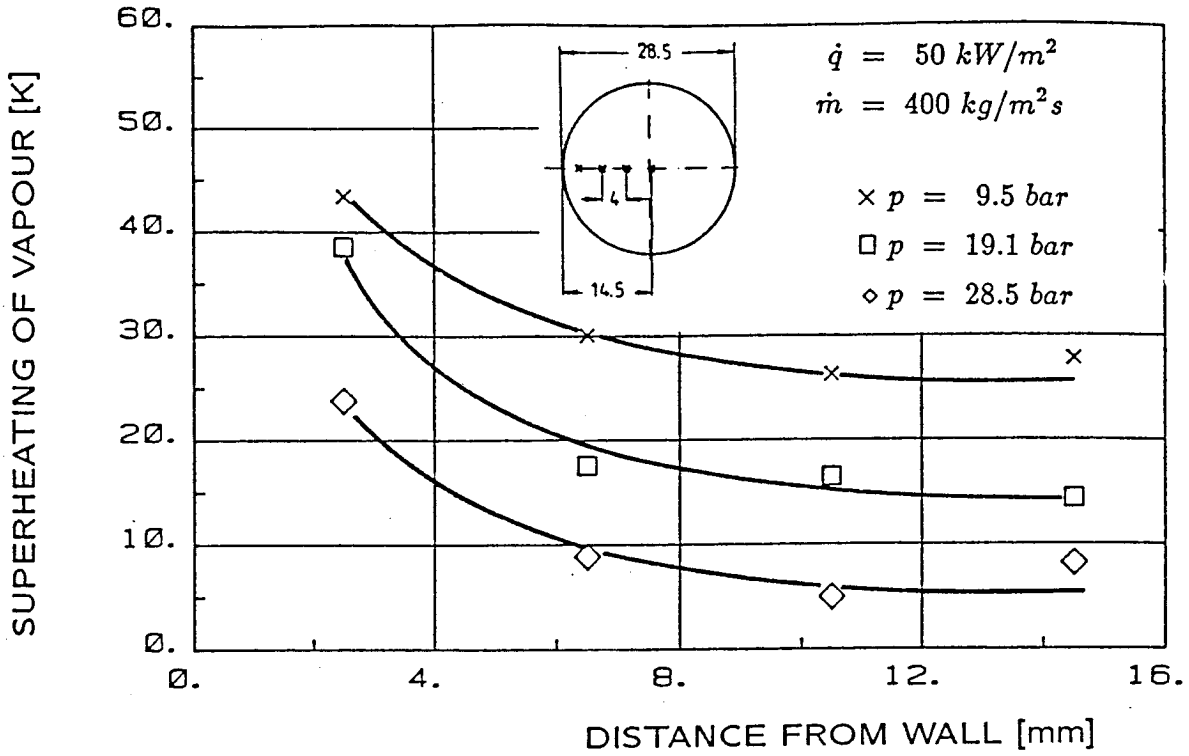

Fig. 13: Influence of pressure upon superheating of vapour

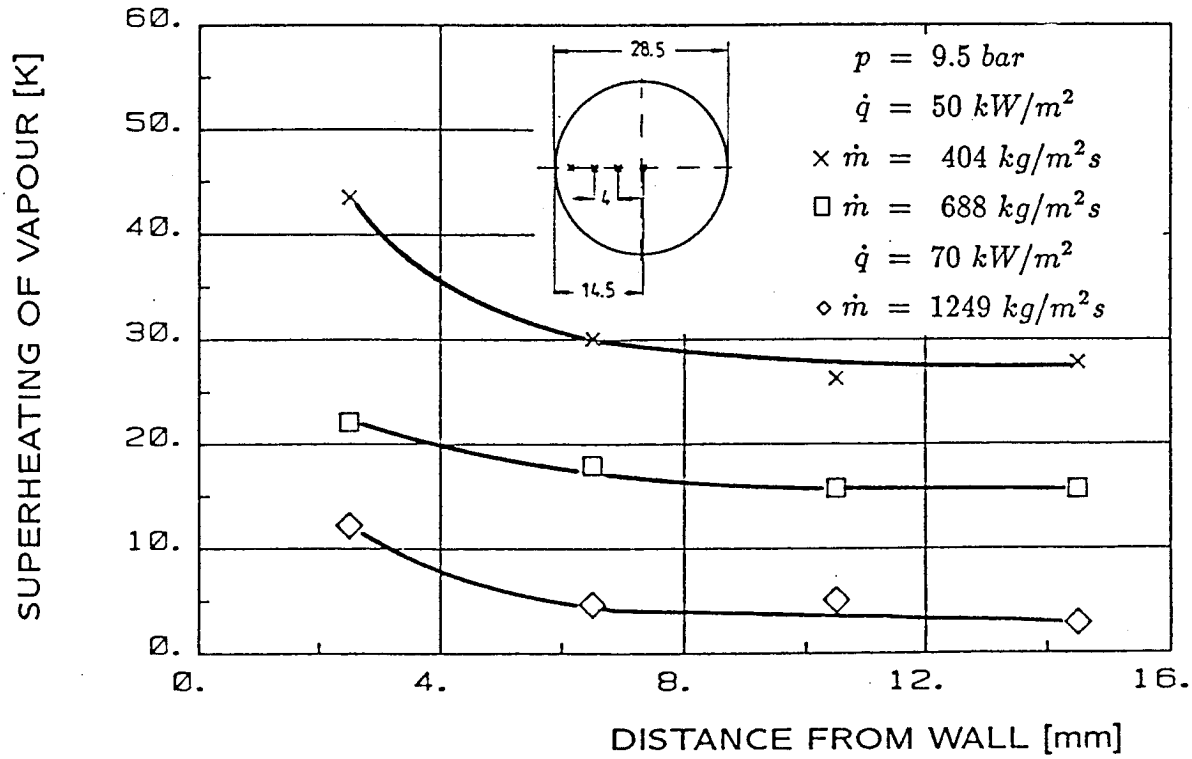

Fig. 14: Influence of mass flow rate upon superheating of vapour

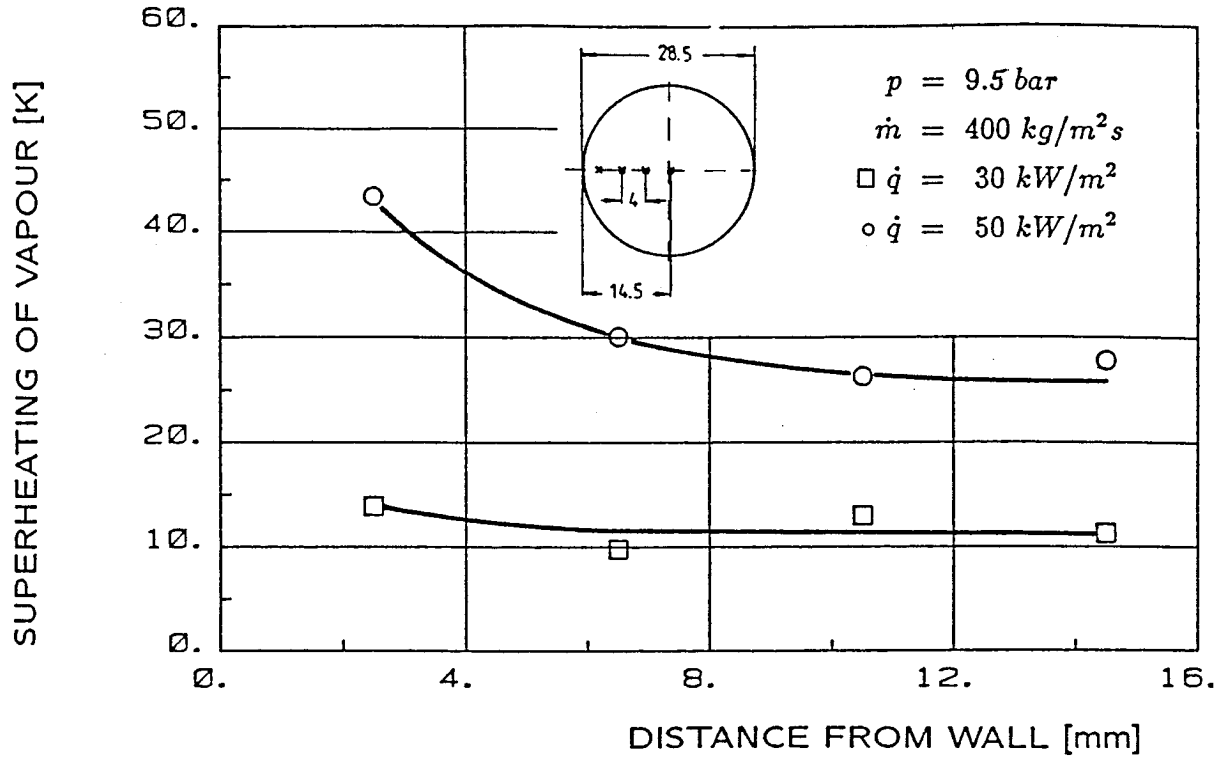

Fig. 15: Influence of heat flux density upon superheating of vapour

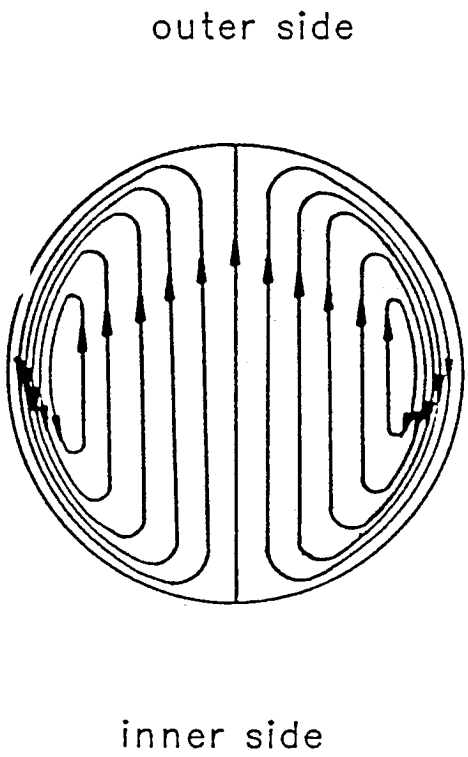

Fig. 16: Streamlines of secondary flow

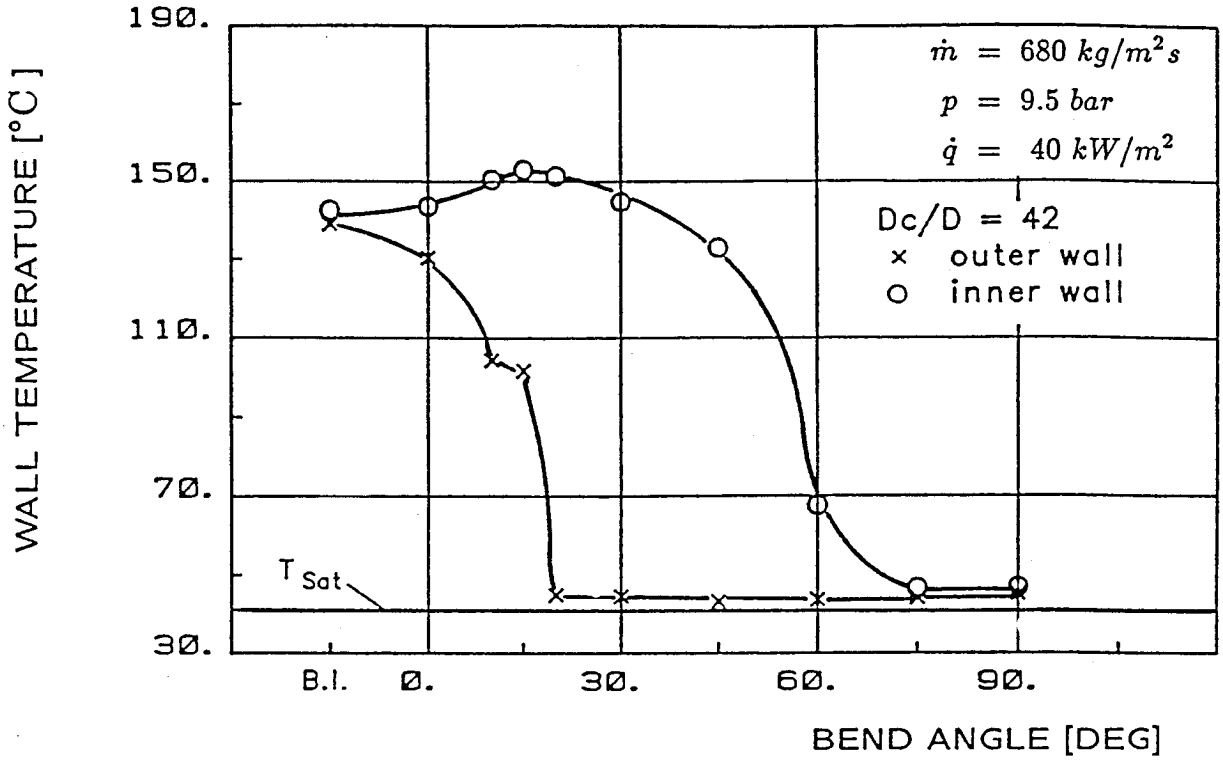

Fig. 17: Wall temperature of the outer and inner side of the bend

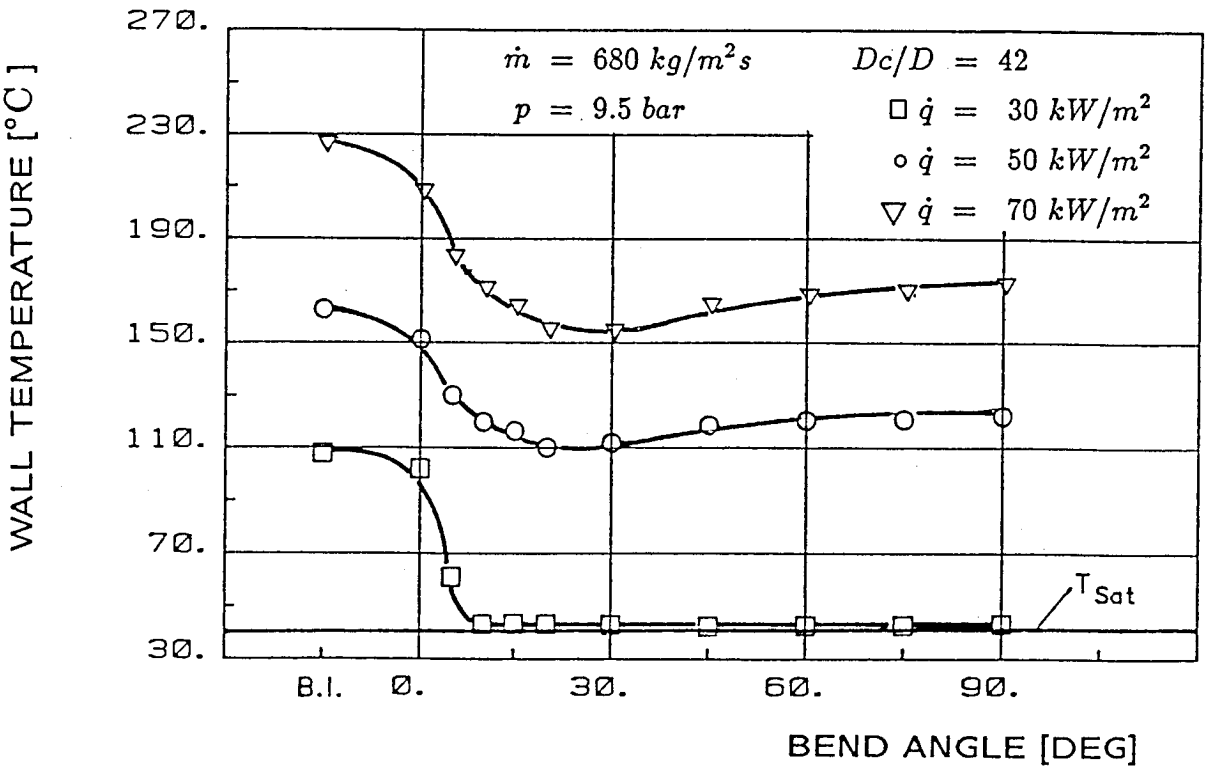

Fig. 18: Influence of heat flux density upon heat transfer at the outer wall of the bend

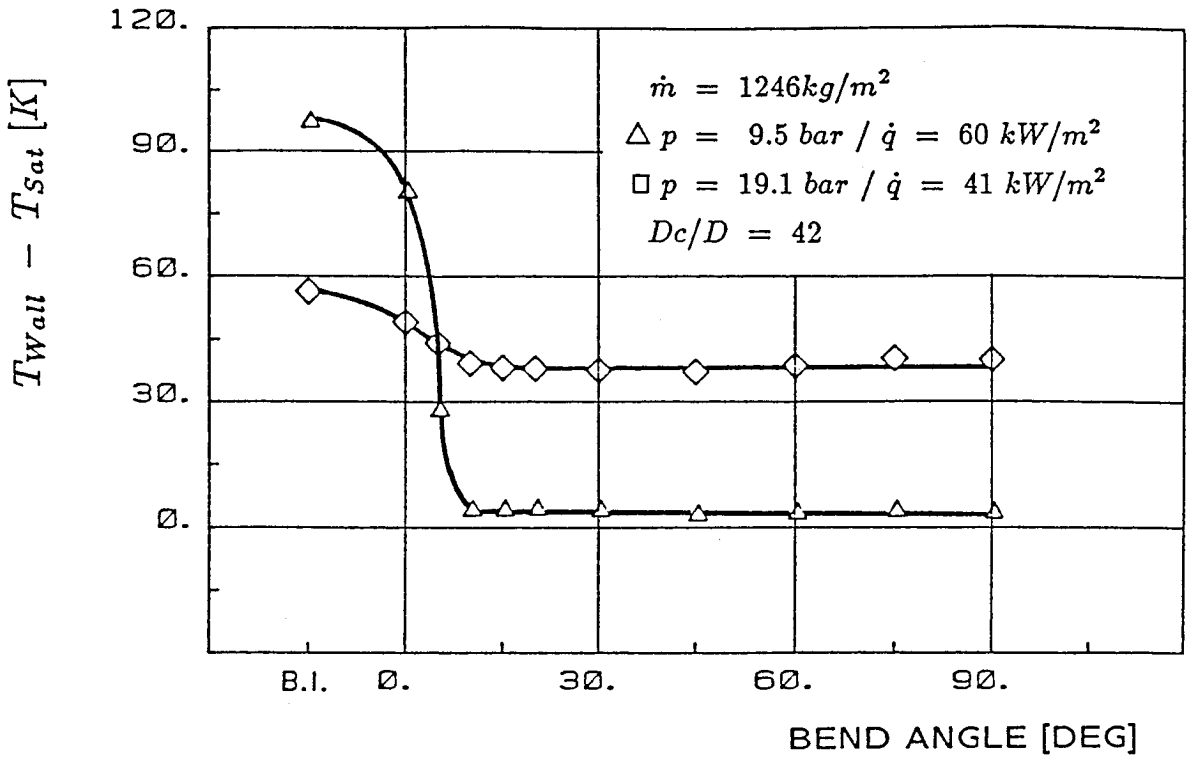

Fig. 19: Influence of pressure upon heat transfer at the outer wall of the bend

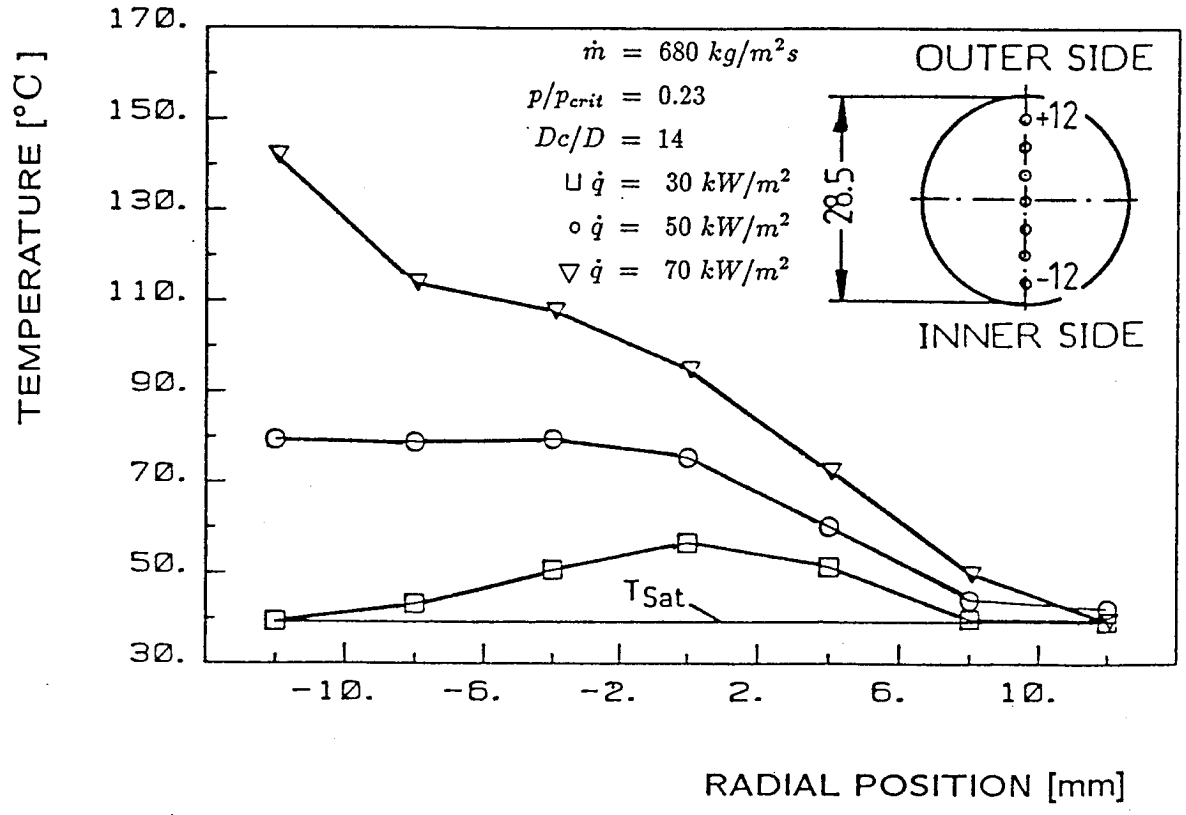

Fig. 21: Vapour temperature profiles after the bend outlet

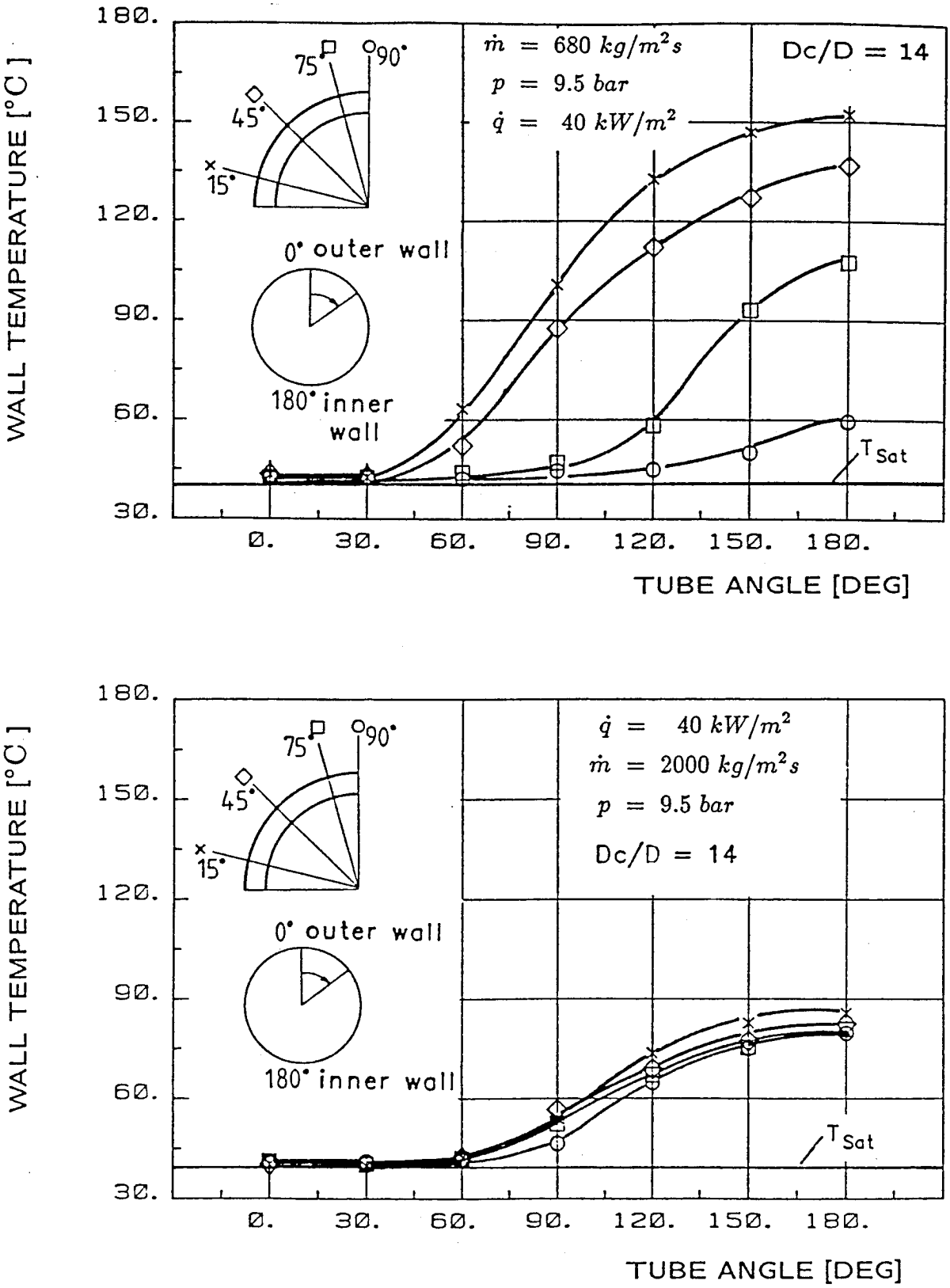

Fig. 20: Influence of mass flow rate upon heat transfer in a bend

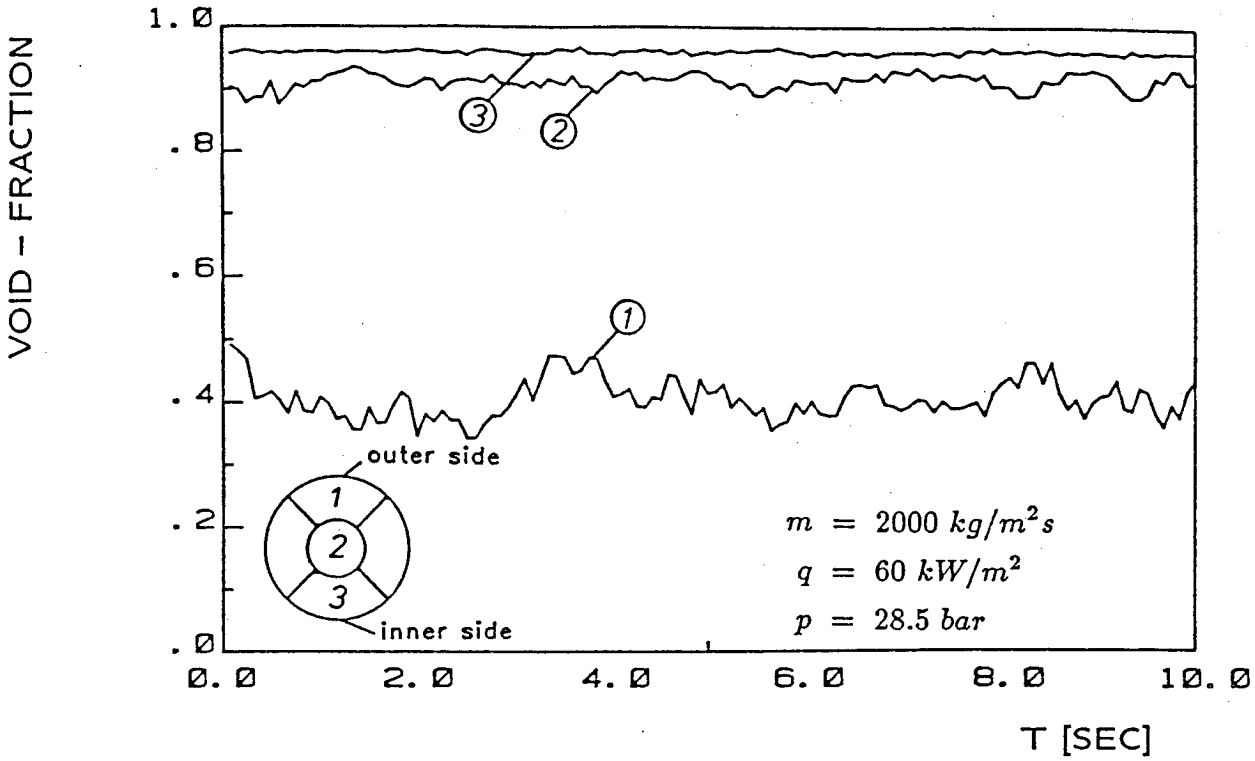

Fig. 22: Void fraction in different areas of the cross section

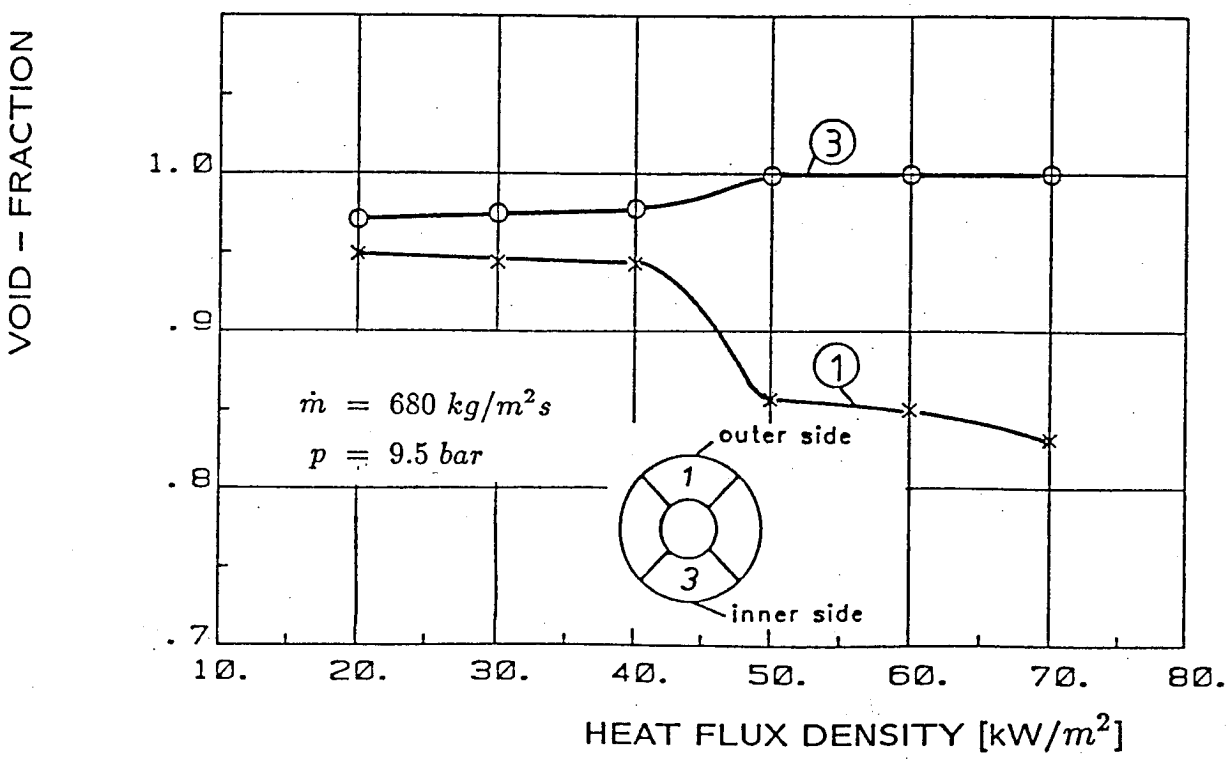

Fig. 23: Time averaged void fractions close to the outer and inner wall of the bend